CHEMISTRY OF MATERIALS

Article

pubs.acs.org/cm

$GeAs_2$: A IV–V Group Two-Dimensional Semiconductor with Ultralow Thermal Conductivity and High Thermoelectric Efficiency

Tianqi Zhao,[†,∥] Yajing Sun,[†,∥] Zhigang Shuai,[†,‡,§] and Dong Wang*[,†]

[†]MOE Key Laboratory of Organic OptoElectronics and Molecular Engineering, Department of Chemistry, Tsinghua University, Beijing 100084, P. R. China

[‡]Key Laboratory of Organic Solids, Beijing National Laboratory for Molecular Science (BNLMS), Institute of Chemistry, Chinese Academy of Science, Beijing 100190, P. R. China

[§]Collaborative Innovation Center of Chemistry for Energy Materials, Xiamen University, Xiamen 351005, P. R. China

Supporting Information

ABSTRACT: The successful demonstration of SnSe single crystals as promising thermoelectric materials highlights alternative strategies to nanostructuring for achieving high thermoelectric efficiency. It stimulates us to screen the periodic table for earth-abundant materials with layered crystal structures and intrinsically low thermal conductivity. $GeAs_2$ is made from group IV and V elements within the same period as selenium, and it exhibits anisotropic and anharmonic bonding character similar to the IV–VI group compound SnSe. Here we present a theoretical investigation of the electronic structure, phonon dispersion, and electron–phonon couplings of monolayer $GeAs_2$ to predict its electrical and thermal transport properties. $GeAs_2$ features flat band and multivalley convergence that give rise to large Seebeck coefficients. Remarkably, monolayer $GeAs_2$ demonstrates anisotropic and amazingly low lattice thermal conductivity of 6.03 W m^{-1} K^{-1} and 0.68 W m^{-1} K^{-1} at 300 K in the *a* and *b* directions, respectively, which we attribute to its soft vibrational modes and anomalously high Grüneisen parameter. The ultralow thermal conductivity leads to maximum thermoelectric figures of merit of 2.1 and 1.8 for n-type and p-type, respectively, at 900 K. These intriguing attributes distinguish $GeAs_2$ from other 2D materials and make it a promising candidate for environmentally friendly thermoelectric applications.

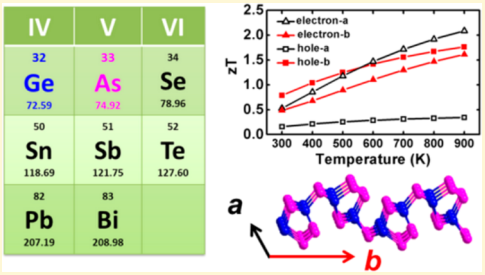

1. INTRODUCTION

The great success of atomically thin graphene[1] has invoked enormous research interests in two-dimensional (2D) materials with potential applications in nanoelectronics,[2] optoelectronics,[3] and thermoelectronics.[4] The rapid progress made in group IV and V elemental analogues[5,6] of graphene, including silicene, stanene, phosphorene, arsenene, and antimonene, leads us to think of such a question as to whether IV–V laminar compounds exist and demonstrate intriguing properties due to combinations of IV and V group elements. We notice that promising thermoelectric materials are made exclusively from V–VI group elements such as Bi_2Te_3 and IV–VI group compounds such as PbTe and SnSe, which share layered crystal structure and possess intrinsically low thermal conductivity.[7] Actually, on the Si–P, Ge–P, Si–As, and Ge–As phase diagrams, semiconducting laminar IV–V group compounds have been known to exist for decades[8,9] yet are ignored by the thermoelectric community. Recently, black plate-like crystals of germanium and germanium–tin phosphides have been prepared by Lee et al.[10] from elements and identified to be semiconductors by combining quantum-mechanical calculations and resistivity measurements. They used the same method to synthesize GeAs and Sn-doped GeAs and found them to be highly anisotropic thermoelectric materials.[11] Barreteau et al.[12] also successfully prepared SiP, SiAs, GeP, and GeAs layered materials by high pressure melt growth and confirmed that all of them exhibited semiconducting behavior and could be cleaved to atomic layers. The record-high thermoelectric figure of merit achieved in SnSe single crystals[13−15] inspires us to investigate the thermoelectric properties of $GeAs_2$ and its 2D counterpart, since $GeAs_2$ is made from group IV and V elements within the same period as selenium and exhibits anisotropic and anharmonic bonding character similar to the IV–VI compound SnSe, which promises an intrinsically low lattice thermal conductivity.[13]

On the phase diagram of Ge and As, $GeAs_2$ melts at 1005 K, below which it adopts an orthorhombic crystal structure with the space group of *Pbam*.[16] Bulk $GeAs_2$ is a van der Waals solid with layered structure. Each layer is composed of $(Ge_2As_3)_n$ pentagonal tubes in the *a* direction and connected by As atoms in the *b* direction (Figure 1a and Figure S1). Each Ge atom exhibits sp^3 hybridization and binds with four As atoms. Although the As atom also shows sp^3 hybridization, it binds with three adjacent atoms, leaving an electron lone pair which helps to separate the layers as well as the pentagonal tubes.[10] In this work, we theoretically discover that $GeAs_2$ is an indirect

Received: March 31, 2017
Revised: July 6, 2017
Published: July 7, 2017

DOI: 10.1021/acs.chemmater.7b01343
Chem. Mater. 2017, 29, 6261−6268

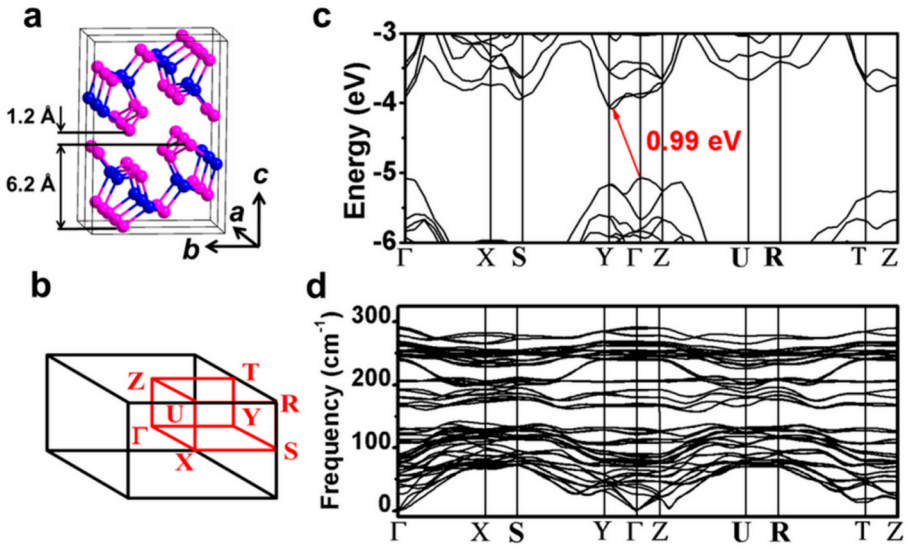

Figure 1. Crystal and electronic structure of bulk $GeAs_2$. (a) Crystal structure of a 2 × 1 × 1 supercell of bulk $GeAs_2$. (b) The First Brillouin zone of bulk $GeAs_2$ with high symmetry points. (c) Electronic band structure of bulk $GeAs_2$. The band energies are absolute energies relative to vacuum. (d) Phonon dispersion of bulk $GeAs_2$.

bandgap semiconductor with band convergence and large Seebeck coefficient, moderate charge mobility, and ultralow lattice thermal conductivity. We demonstrate that it is stable in a single layer by phonon dispersion, cleavage cohesive energy, and high temperature molecular dynamics. The bandgap of $GeAs_2$ remains indirect when thinned from bulk to monolayer, but it increases from 0.99 to 1.64 eV due to the quantum confinement effect. Monolayer $GeAs_2$ has moderate electron mobility of 224 $cm^2\ V^{-1}\ s^{-1}$ and 41 $cm^2\ V^{-1}\ s^{-1}$ and ultralow lattice thermal conductivity of 6.03 $W\ m^{-1}\ K^{-1}$ and 0.68 $W\ m^{-1}\ K^{-1}$ in the *a* and *b* directions, respectively, at room temperature. The remarkably high figure of merit of $GeAs_2$ at 900 K (n-type 2.1 and p-type 1.8) is attributed to its intrinsically ultralow lattice thermal conductivity. $GeAs_2$ features soft vibrational modes and anomalously high Grüneisen parameters that reflect its highly anharmonic and anisotropic bonding. These unique features are responsible for the exceptionally low thermal conductivity, which makes $GeAs_2$ a very promising earth-abundant candidate for applications in thermoelectrics.

2. METHODS

2.1. DFT and DFPT Calculations. DFT calculations were performed by using the projector augmented wave (PAW) method and the Perdew–Burke–Ernzerhof (PBE) exchange-correlation functional as implemented in the Vienna Ab initio Simulation Package (VASP).[17,18] The Grimme's D3 method[19] was used to account for the inter- and intralayer van der Waals interactions. A plane-wave basis set of 700 eV was adopted for all the calculations. The Monkhorst–Pack **k**-meshes of 14 × 6 × 4 and 15 × 6 × 1 were used for sampling the Brillouin zone of bulk and monolayer $GeAs_2$, respectively. The total energy was converged to 10^{-6} eV, and the force on either atom in either direction was converged to less than 0.001 eV/ Å. The crystal structure was optimized by monitoring the stress in either crystal direction to less than 0.02 kbar. The band structure was calculated by using the HSE06 hybrid functional[20] based on the optimized structure. The phonon dispersion relations for monolayer and bulk $GeAs_2$ were obtained by performing density functional perturbation theory (DFPT) calculations as implemented in Quantum Espresso.[21] The norm-conserving pseudopotentials with local density approximation (LDA) were used for Ge and As atoms. The cutoff energy for the plane-waves basis set was 80 Ry. The **k**-meshes of 7 × 3 × 2 and 7 × 3 × 1 were used to converge the electron density for bulk and monolayer $GeAs_2$, respectively. The same **q**-meshes of 7 × 3 × 2 and 7 × 3 × 1 were applied for bulk and monolayer $GeAs_2$, respectively.

2.2. Electrical Transport Property Calculation. Electrical conductivity σ, Seebeck coefficient S, and electrical thermal conductivity κ_e were calculated by solving the Boltzmann transport equation:

$$\sigma = \frac{e^2}{\Omega}\int \tau(\mathbf{k})\mathbf{v}(\mathbf{k})\mathbf{v}(\mathbf{k})\left(-\frac{\partial f^0(\varepsilon_k)}{\partial \varepsilon_k}\right)\mathrm{d}\varepsilon \quad (1)$$

$$S = \frac{e}{\sigma T\Omega}\int \tau(\mathbf{k})\mathbf{v}(\mathbf{k})\mathbf{v}(\mathbf{k})(\varepsilon_k - \varepsilon_F)\left(-\frac{\partial f^0(\varepsilon_k)}{\partial \varepsilon_k}\right)\mathrm{d}\varepsilon \quad (2)$$

$$\kappa_e = \frac{1}{\Omega}\int \tau(\mathbf{k})\mathbf{v}(\mathbf{k})\mathbf{v}(\mathbf{k})\frac{(\varepsilon_k - \varepsilon_F)^2}{T}\left(-\frac{\partial f^0(\varepsilon_k)}{\partial \varepsilon_k}\right)\mathrm{d}\varepsilon - S^2\sigma T \quad (3)$$

where ε_k, $\mathbf{v}(\mathbf{k})$, and $\tau(\mathbf{k})$ are the electronic energy, group velocity, and relaxation time, respectively, of electrons with wave-vector **k**. e is the elementary charge, T is the absolute temperature, and $f^0(\varepsilon_k)$ is the Fermi–Dirac distribution. Here we mimic the doping process by adopting the rigid band approximation and simply shifting the Fermi level ε_F in the Fermi–Dirac distribution function. The carrier concentration n is determined by the electronic band structure and the Fermi–Dirac distribution function with two control parameters in it, the temperature T, and the Fermi level ε_F. The charge carrier mobility μ is derived by the relation $\sigma = \mu en$ at low carrier concentrations n. Ω is the volume of the unit cell. It should be noted that, for 2D materials, $\Omega = Ah_{eff}$, where A is the area of unit cell and h_{eff} is the effective thickness of the 2D material. h_{eff} is often chosen as the interlayer distance in the bulk counterpart of the 2D material. The interlayer distance in bulk $GeAs_2$ (h_{eff} = 7.404 Å) is chosen in our calculation to convert conductance of monolayer $GeAs_2$ to conductivity. h_{eff} is a measure of the confinement of charge carriers in the perpendicular direction of the 2D material, and our choice is also justified by the cleavage cohesive energy, which converges when the interlayer distance is larger than 7 Å as will be shown below. It should be noted that we use the same effective thickness for both electrical and phonon transport property calculations, and the result of the thermoelectric figure of merit zT will not be affected by our choice. The group velocity $\mathbf{v}(\mathbf{k})$ was calculated from the expectation value of the velocity operator as implemented in the EPW package.[22] The

DOI: 10.1021/acs.chemmater.7b01343
Chem. Mater. 2017, 29, 6261–6268

relaxation time was calculated by applying the Fermi's golden rule and fully incorporating scatterings from all of the phonon modes as

$$\frac{1}{\tau_{n\mathbf{k}}} = \frac{2\pi}{\hbar}\sum_{n',\lambda\mathbf{q}} |g_{\lambda q}(\mathbf{k}, n, n')|^2(1-\cos\theta_{\mathbf{k},\mathbf{k}+\mathbf{q}}) \{(f^0_{n'\mathbf{k}+\mathbf{q}} + n^0_{\lambda\mathbf{q}})\delta(\varepsilon_{n'\mathbf{k}+\mathbf{q}} - \varepsilon_{n\mathbf{k}} - \hbar\omega_{\lambda\mathbf{q}}) + (1 + n^0_{\lambda\mathbf{q}} - f^0_{n'\mathbf{k}+\mathbf{q}})\delta(\varepsilon_{n'\mathbf{k}+\mathbf{q}} - \varepsilon_{n\mathbf{k}} + \hbar\omega_{\lambda\mathbf{q}})\} \quad (4)$$

where n and $\mathbf{k}$ are the band index and wave-vector of an electronic state and λ and $\mathbf{q}$ are the mode index and wave-vector of the phonon emitted or absorbed in scatterings. $\mathbf{k}+\mathbf{q}$ is the wave-vector of the final electronic state. $\varepsilon_{n'\mathbf{k}+\mathbf{q}}$, $\varepsilon_{n\mathbf{k}}$, and $\hbar\omega_{\lambda\mathbf{q}}$ are the corresponding energies of electrons and phonons involved in the scattering. $n^0_{\lambda\mathbf{q}}$ is the Bose–Einstein distribution of phonons, and $f^0_{n'\mathbf{k}+\mathbf{q}}$ is the Fermi–Dirac distribution of the final electronic state. $\theta_{\mathbf{k},\mathbf{k}+\mathbf{q}}$ is the scattering angle between the initial and final electronic states. In the framework of DFPT, the electron–phonon coupling matrix element $g_{\lambda\mathbf{q}}(\mathbf{k}, n, n')$ is expressed as

$$g_{\lambda\mathbf{q}}(\mathbf{k}, n, n') = \sqrt{\frac{\hbar}{2\omega_{\lambda q}}}\langle\psi_{n'\mathbf{k}+\mathbf{q}}|\Delta V^{\lambda q}_{KS}|\psi_{n\mathbf{k}}\rangle \quad (5)$$

where $\Delta V^{\lambda q}_{KS}$ the self-consistent first-order derivative of Kohn–Sham potential. $|\psi_{n\mathbf{k}}\rangle$ and $|\psi_{n'\mathbf{k}+\mathbf{q}}\rangle$ are initial and final Bloch functions, respectively. $\hbar$ is the reduced Planck constant. The DFT and DFPT calculations as implemented in the Quantum Espresso[21] package were used to obtain the band structure, phonon dispersion, and electron–phonon coupling matrix of monolayer $GeAs_2$ on an initial coarse $\mathbf{k}$- and $\mathbf{q}$-mesh of 7 × 3 × 1. Then the EPW[22] package was used to interpolate the electronic band structure, phonon dispersion, and electron–phonon coupling matrix on a fine $\mathbf{k}$- and $\mathbf{q}$-mesh of 210 × 90 × 1 based on the Maximally Localized Wannier Function method.[23]

2.3. Lattice Thermal Conductivity Calculation. κ_L was calculated by solving the Boltzmann equation of phonons[24]

$$\kappa_L = \sum_{\lambda}^{3N}\int_{\mathbf{q}} \mathbf{v}_{\lambda\mathbf{q}}{}^2 c_{\lambda\mathbf{q}}\tau_{\lambda\mathbf{q}}\,\mathrm{d}\mathbf{q} \quad (6)$$

where $\boldsymbol{v}_{\lambda\mathbf{q}}$, $c_{\lambda\mathbf{q}}$, and $\tau_{\lambda\mathbf{q}}$ are the phonon group velocity, the mode-specific heat capacity, and the relaxation time, respectively, for a phonon with the wave-vector $\mathbf{q}$ and mode λ. $\boldsymbol{v}_{\lambda\mathbf{q}}$ and $c_{\lambda\mathbf{q}}$ are calculated as

$$\mathbf{v}_{\lambda\mathbf{q}} = \frac{\partial\omega_{\lambda\mathbf{q}}}{\partial\mathbf{q}};\ c_{\lambda\mathbf{q}} = \frac{k_B}{\Omega}\frac{x^2e^x}{(e^x-1)^2};\ x = \frac{\hbar\omega_{\lambda\mathbf{q}}}{k_BT} \quad (7)$$

where k_B is the Boltzmann constant. The phonon relaxation time was derived by the Callaway model describing resistive Umklapp phonon–phonon scatterings[25]

$$\tau_{\lambda\mathbf{q}}{}^{-1} = \frac{\hbar\gamma^2_{\lambda\mathbf{q}}}{\bar{M}\Theta_\lambda v_{\lambda\mathbf{q}}{}^2}\omega_{\lambda\mathbf{q}}{}^2Te^{-\Theta_\lambda/3T} \quad (8)$$

where $\gamma_{\lambda\mathbf{q}}$ is the Grüneisen parameter, $\bar{M}$ is the average atomic mass of the unit cell, and Θ_λ is the mode-specific Debye temperature

$$\Theta_\lambda{}^2 = \frac{5\hbar^2}{3k_B{}^2}\frac{\int\omega^2 g_\lambda(\omega)\,\mathrm{d}\omega}{\int g_\lambda(\omega)\,\mathrm{d}\omega} \quad (9)$$

with $g_\lambda(\omega) = \sum_{\mathbf{q}}\delta[\omega - \omega_{\lambda\mathbf{q}}]$ the vibrational density of states of mode λ. The Grüneisen parameter reflects the anharmonicity and phonon–phonon scattering strength, and it can be estimated by[26]

$$\gamma_{\lambda\mathbf{q}} = -[A/\omega_{\lambda\mathbf{q}}][\mathrm{d}\omega_{\lambda\mathbf{q}}/dA] \quad (10)$$

with A the cell area of monolayer $GeAs_2$. On the basis of DFPT calculations at a series of cell areas, Grüneisen parameters for all phonon modes and phonon dispersions were derived with the Phonopy[27] code.

3. RESULTS AND DISCUSSION

3.1. Geometric and Electronic Properties of Bulk and Monolayer $GeAs_2$. We start by benchmarking theoretical methods with crystal and electronic structure of bulk $GeAs_2$. In the structure relaxation of bulk $GeAs_2$, we use different functionals to account for inter- and intralayer van der Waals interactions (Table S1). The lattice constants of $GeAs_2$ single crystal predicted by PBE+D3 functional (a = 3.788 Å, b = 10.286 Å, c = 14.808 Å) agree well with the experimental data (a = 3.728 Å, b = 10.16 Å, c = 14.76 Å).[16] The layer thickness and interlayer distance are calculated to be 6.2 and 1.2 Å, respectively (Figure 1a). Excellent agreement has been obtained between the theoretical and the experimental bond lengths and angles (Table S2). Since bandgaps are often underestimated by DFT calculations based on the generalized gradient approximation (GGA), we further calculate its band structure by adopting the HSE06 functional,[20] which incorporates 20% exact Hartree–Fock exchange interaction and has been shown to give better description of bandgaps for semiconductors.[28] Bulk $GeAs_2$ is predicted to be an indirect bandgap semiconductor with a bandgap of 0.99 eV (Figure 1c), which agrees excellently with the experimental value of 1.06 eV.[9] The above results demonstrate that PBE+D3 combined with the HSE06 functional is a reasonable choice of theoretical model to investigate electronic properties of $GeAs_2$ and its 2D counterpart.

The successful preparation of mono- and few-layer $GeAs_2$ is prerequisite to exploring its electronic properties experimentally. Free-standing graphene, boron nitride, phosphorene, and atomically thin transition metal dichalcogenides have been fabricated by micromechanical cleavage or liquid exfoliation methods.[29,30] Here we confirm that it is feasible to exfoliate $GeAs_2$ thin layers by modeling the cleavage process:[31] a fracture of the bulk (four layers in total) is introduced to show the variation of total energy with the distance d between the top layer and the remaining three layers (Figure 2a). The calculated

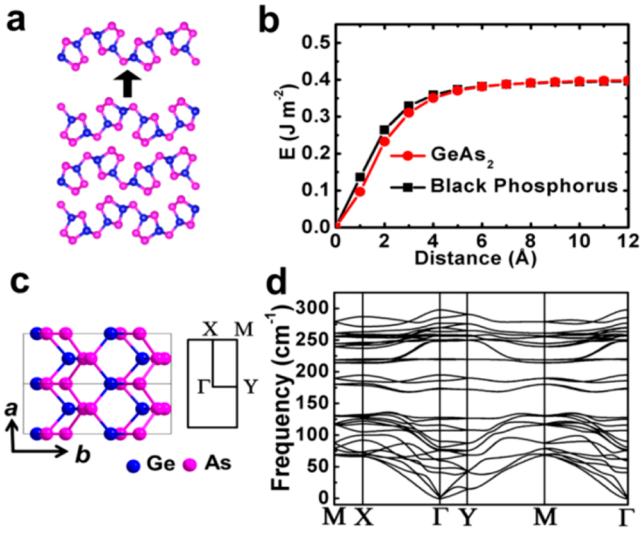

Figure 2. Stability of monolayer $GeAs_2$. (a) Schematic view of the cleavage process of monolayer $GeAs_2$ from bulk. (b) Cleavage cohesive energy as a function of the distance between a top layer and bottom layers of $GeAs_2$. The cleavage of black phosphorus is also plotted for comparison. (c) Top view of a 2 × 1 supercell of monolayer $GeAs_2$ (left) and the First Brillouin zone with high symmetry point highlighted (right). (d) Phonon dispersion of monolayer $GeAs_2$.

DOI: 10.1021/acs.chemmater.7b01343
Chem. Mater. 2017, 29, 6261–6268

cleavage cohesive energy of $GeAs_2$ is 0.40 J m^{-2} (Figure 2b), close to that of black phosphorus, which is 0.40 J m^{-2} calculated by us and 0.36 J m^{-2} according to a previous calculation.[32] This indicates that atomically thin layers of $GeAs_2$ can be prepared by mechanical or liquid exfoliation methods.

The relaxed structure of monolayer $GeAs_2$ (with a = 3.758 Å, b = 10.388 Å) retains the waved feature of bulk $GeAs_2$ (Figure 2c). The lattice parameter b increases by 0.1 Å as compared to its bulk value, which can be ascribed to the freeing of monolayer $GeAs_2$ from interlayer interactions. We study the dynamical stability of monolayer $GeAs_2$ by calculating its phonon dispersion, since negative frequency in phonon dispersion is a sign of instability arising from the softening of lattice vibrations.[6] The phonon dispersion of monolayer $GeAs_2$ shows no appreciable negative frequency, indicating that monolayer $GeAs_2$ is dynamically stable (Figure 2d). We further corroborate the stability of monolayer $GeAs_2$ by performing ab initio molecular dynamic simulations at medium to high temperatures. The radical distribution functions (RDF, Figure S2) at 300 and 1000 K show the typical feature of the solid. At 1500 K, the RDF exhibits the typical feature of liquid. This indicates that monolayer $GeAs_2$ has a melting temperature similar to that of bulk $GeAs_2$.

The electronic band structure of monolayer $GeAs_2$ is plotted in Figure 3a. It is an indirect bandgap semiconductor with

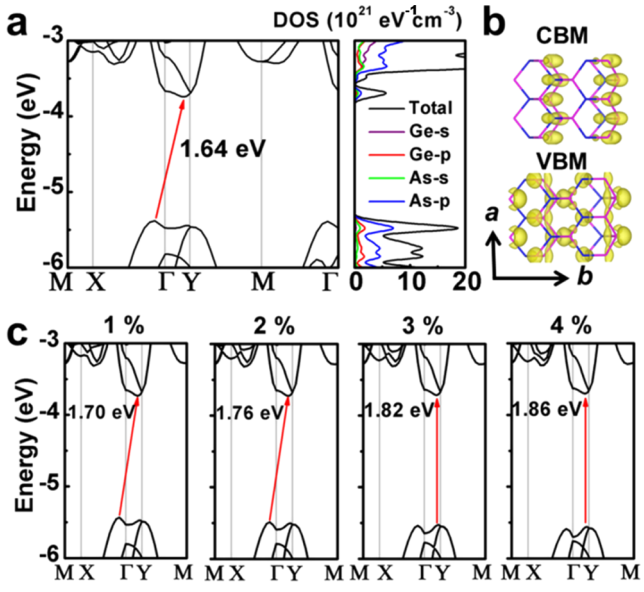

Figure 3. Electronic properties of monolayer $GeAs_2$. (a) Electronic band structure and density of states (DOS). (b) Electron density distribution at CBM and VBM. (c) Electronic band structure evolution under 1%, 2%, 3%, and 4% uniaxial tensile strains along the b axis. The band energies in (a) and (c) are absolute energies relative to vacuum.

bandgap of 1.64 eV. The valence band maximum (VBM) is located along the Γ−X high symmetry line, while the conduction band minimum (CBM) is located on the Γ−Y high symmetry line and close to Y. The density of states (DOS) near band edges is mainly contributed by the p-orbital of As (Figure 3a and Figure 3b). The bandgap of 1.64 eV corresponds to 756 nm, implying that monolayer $GeAs_2$ can absorb all visible lights. As monolayer MoS_2 transistor has a large on/off ratio due to its bandgap of 1.8 eV,[33] transistor made from monolayer $GeAs_2$ may also have a large on/off ratio. The large bandgap also helps to reduce the gate-induced drain leakage in field-effect-transistors (FET).[34] The absolute energy levels of VBM and CBM relative to vacuum (Figure S3 and Methods in Supporting Information) are −5.38 eV and −3.74 eV, respectively. Metals with work functions similar to the band edge energies of semiconductors usually form a smaller Schottky barrier, which results in lower contact resistance and higher carrier injection.[35] The energy of CBM of monolayer $GeAs_2$ is found to be close to the work functions of Ag (−4.2 eV) and Sc (−3.5 eV), and that of VBM is slightly lower than the work function of the Au and Pd electrode (−5.2 eV). Therefore, we propose to use Ag or Sc as an electrode in n-type transistors and Au or Pd as an electrode in p-type FETs made of monolayer $GeAs_2$.

The strain effects have been demonstrated as an important method to tune the electronic properties of 2D semiconductors.[36] Experimentally, uniaxial strains can be applied by a three-point or four-point bending apparatus.[37,38] We explore effects of uniaxial strains on the electronic band structure of monolayer $GeAs_2$. The uniaxial strain is applied by straining in one crystal direction, meanwhile relaxing the stress in the perpendicular direction to be less than 0.1 kbar (Figure S4 and Methods in Supporting Information). Under uniaxial tensile strains along the b axis, band dispersion in the Γ−Y direction changes gradually and an indirect-to-direct bandgap transition is observed at a tensile strain between 2% and 3% (Figure 3c). Such strain-induced indirect-to-direct bandgap transition may increase the luminescence efficiency of monolayer $GeAs_2$, as observed in monolayer MoS_2.[39] However, the bandgap of monolayer $GeAs_2$ remains indirect under compressive strains along the b axis up to −3% (Figure S5) and uniaxial strains between −3% and 3% along the a axis (Figure S6).

3.2. Thermoelectric Transport Properties of Monolayer $GeAs_2$. In the following, we report our results of the charge mobility of monolayer $GeAs_2$ obtained by solving the Boltzmann transport equation for charge carriers in the relaxation time approximation. We use the DFPT and Wannier interpolation method to calculate the electron−phonon coupling matrix elements and then apply the Fermi's golden rule to derive the relaxation time of charge carriers by including scatterings with all phonon modes. The deformation potential (DP) theory,[40] which models the electron and longitudinal acoustic (LA) phonon scattering in the long wavelength limit, has been widely applied to predicting charge transport properties of 2D materials, including graphene,[41] graphdiyne,[42] monolayer MoS_2,[43] black phosphorene,[44] and monolayer TiS_3,[45] but it usually overestimates the mobility by a few times due to the neglect of scatterings with other phonon modes. Our results show that acoustic phonon and optical phonon scatterings contribute equally to charge transport in monolayer $GeAs_2$. The overall mobility and the contributions by optical and acoustic phonon scatterings are listed in Table 1. Both transverse acoustic (TA) and LA phonons play a significant role in charge scatterings, and out-of-plane acoustic (ZA) phonon mode is less important (Table S3). The anisotropy of mobility μ is mainly determined by the anisotropy of effective mass m^*. Both electrons and holes have smaller effective mass along the a axis (Table 1), which is evident by viewing the dispersive band along the Γ−X direction (a-axis) and the nearly flat band along Γ−Y direction (b-axis) in Figure 3a. As a result, mobilities of both electrons and holes are larger along the a axis. The effective mass of electrons is smaller than holes, so the mobility of electrons is higher than holes (Table

DOI: 10.1021/acs.chemmater.7b01343
Chem. Mater. 2017, 29, 6261−6268

Table 1. Effective Masses m^*, Relaxation Times τ, Mean Free Paths l, and Mobilities μ of Charge Carriers in Monolayer $GeAs_2$ at 300 K[a]

	electron		hole	
direction	*a*	*b*	*A*	*b*
m^*/m_e	0.27	1.11	0.88	1.06
τ (fs)	23		27	
l (nm)	3.3		2.2	
μ ($cm^2\ V^{-1}\ s^{-1}$)	224	41	53	39
μ_{OP} ($cm^2\ V^{-1}\ s^{-1}$)	420	62	140	106
μ_{AC} ($cm^2\ V^{-1}\ s^{-1}$)	519	139	87	65

[a]The mobilities arising from optical phonon and acoustic phonon scatterings, μ_{OP} and μ_{AC}, are displayed, respectively.

1). The highest room-temperature (300 K) electron mobility of monolayer $GeAs_2$ is predicted to be 224 $cm^2\ V^{-1}\ s^{-1}$ along the *a* axis, which is comparable to monolayer MoS_2 (~200 $cm^2\ V^{-1}\ s^{-1}$).[2]

The flat bands in the *b* (Γ−Y) direction and nearly degenerate valleys at VBM and Y (Figure 3a) promise large Seebeck coefficient and high thermoelectric power factor. For enhanced thermoelectric efficiency, doping optimization is usually indispensable to increase the carrier concentration and attain high electrical conductivity. The Seebeck coefficient *S*, electrical conductivity σ, thermoelectric power factor $S^2\sigma$, and electrical thermal conductivity κ_e as a function of carrier concentration have been shown in Figure 4. At 300 K, the Seebeck coefficient of holes is +284 $\mu V\ K^{-1}$ and that of electron is −276 $\mu V\ K^{-1}$ at the carrier concentration of 4×10^{19} cm^{-3}. These values are higher than that of Na-doped SnSe single crystal (+160 $\mu V\ K^{-1}$), which was reported to have a thermoelectric figure of merit 0.7 at the same temperature and carrier concentration.[14] Since *S* decreases while σ increases with the carrier concentration, the power factor of electrons has a maximum of 139 $\mu W\ cm^{-1}\ K^{-2}$ along the *a* axis at the carrier concentration of 1.7×10^{20} cm^{-3} (Figure 4a and Table S4). The maximum power factor for holes is 33 $\mu W\ cm^{-1}\ K^{-2}$ along the *a* axis at the carrier concentration of 1.2×10^{20} cm^{-3} (Figure 4b and Table S4).

3.3. Lattice Thermal Conductivity of Monolayer $GeAs_2$.

The remarkably high thermoelectric figure of merit realized in SnSe single crystals has been attributed to its intrinsically ultralow lattice thermal conductivity.[13] $GeAs_2$ is composed of group IV and V elements within the same period as selenium, and it shares layered structure and complex bonding character similar to the IV−VI group compound SnSe. The in-plane lattice thermal conductivity of monolayer $GeAs_2$ is predicted by solving the Boltzmann transport equation for phonons within the relaxation time approximation. The phonon lifetime and thermal conductivity are determined predominantly by phonon−phonon scatterings, which arise from anharmonic lattice vibrations. The strength of lattice anharmonicity can be characterized by Grüneisen parameters, which are estimated from the phonon frequency change with respect to crystal volume change (see eq 10 in Methods). The in-plane lattice thermal conductivity of $GeAs_2$ is highly anisotropic, in accord with its anisotropic crystal structure featured with pentagonal $(Ge_2As_3)_n$ tubes in the *a* direction and connected by As atoms in the *b* direction. The room-temperature (300 K) lattice thermal conductivity is 0.68 W $m^{-1}\ K^{-1}$ along the *b* axis, one order-of-magnitude lower than that along the *a* axis, which is 6.03 W $m^{-1}\ K^{-1}$. We attribute this anisotropy to the anisotropic phonon dispersion relations (Figure S7a), in which acoustic phonon modes in the Γ−Y direction (*b* axis) are significantly softer, with lower Debye temperatures and smaller group velocities (Table 2), than those in the Γ−X direction (*a* axis). The Debye temperature of three acoustic phonon modes in monolayer $GeAs_2$, especially those along the *b* axis (with the average value of 6.9 K, Table 2), are significantly lower than those in SnSe single crystals (with the average values of 24, 65, and 58 K along the *a*, *b*, and *c* axes in low-temperature SnSe phase).[13] These soft modes along the *b* axis also suggest possible strong anharmonicity. We plot the dispersion of the Grüneisen parameters for LA, TA, and ZA phonon modes of monolayer $GeAs_2$ (Figure S7b), which shows that the Grüneisen parameters along the *b* axis (with the average value of 10.0) are indeed larger than those along the *a* axis (with the average value of 4.3, Table 2). The ZA Grüneisen parameters are largest among the three acoustic phonon

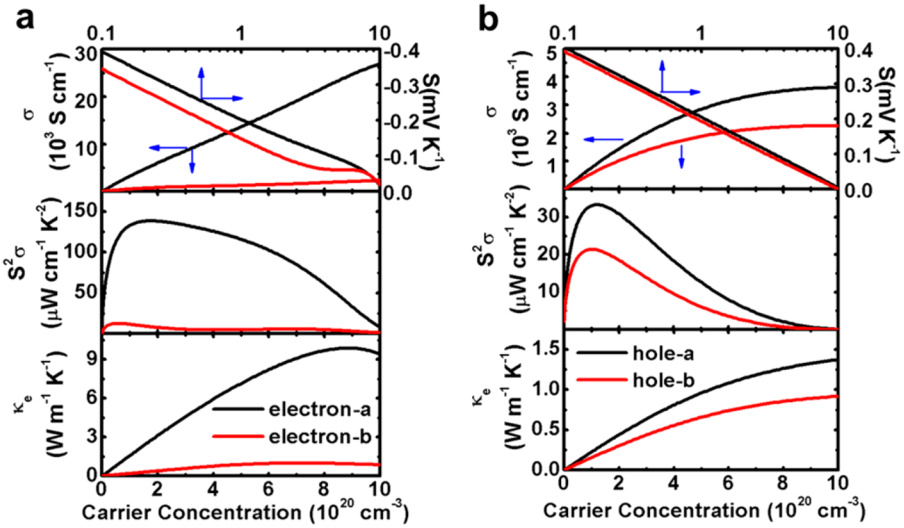

Figure 4. Electronic conductivity σ, Seebeck coefficient *S*, power factor $S^2\sigma$, and electronic thermal conductivity κ_e of monolayer $GeAs_2$ as a function of carrier concentration at 300 K: (a) electrons and (b) holes.

DOI: 10.1021/acs.chemmater.7b01343
Chem. Mater. 2017, 29, 6261−6268

Table 2. Debye Temperature (Θ), Phonon Velocities (v), and Grüneisen Parameter (γ) along the *a* and *b* Axes in Monolayer $GeAs_2$[a]

ΓX/*a*	Θ (K)	*v* (m/s)	γ
ZA	18.1	111	7.1
TA	19.8	1325	2.3
LA	19.9	2823	3.5
average	19.3	1420	4.3
ΓY/*b*	Θ (K)	*v* (m/s)	γ
ZA	3.7	91	15.5
TA	6.6	1094	6.3
LA	10.4	1400	8.1
average	6.9	861	10.0

[a]These values are calculated from the phonon and Grüneisen dispersion (Figure S7). The Debye temperature is estimated by $\Theta = \omega_D/k_B$ (with ω_D the highest phonon frequency in each direction); the phonon velocity is the slope of the acoustic phonon dispersion around the Γ point; the Grüneisen parameter is evaluated from the root-mean-square value of γ_λ (**q**) (see eq 10 in Methods) along each direction.

branches, with the maximum extraordinarily high (~20) around the Γ point. The Grüneisen parameters for optical phonon modes, both longitudinal and transverse (LO and TO), are much smaller (Figure S8), indicating that contribution of optical phonons to the thermal resistivity are negligibly small. The maximum Grüneisen parameter of SnSe is ~7.2,[13] corresponding to the measured thermal conductivities at room temperature of ~0.46, 0.70, and 0.68 W m^{-1} K^{-1} along the *a*, *b*, and *c* axis directions. In contrast to SnSe single crystals which exhibit isotropic in-plane lattice thermal conductivity, $GeAs_2$ shows 10-fold anisotropy owing to its highly anisotropic in-plane bonding character. The soft vibrational modes and anomalously high anharmonicity in $GeAs_2$ therefore lead to exceptionally low lattice thermal conductivity along the *b* axis.

The moderate mobility, large Seebeck coefficient, and ultralow lattice thermal conductivity make $GeAs_2$ a promising candidate for environmentally friendly thermoelectric applications. Indeed, the maximum thermoelectric figures of merit for electrons at room temperature are predicted to be 0.53 and 0.48 in the *a* and *b* axis directions at the carrier concentrations of 8.6×10^{19} cm^{-3} and 4.4×10^{19} cm^{-3}, respectively, and that for holes is 0.16 and 0.79 at the carrier concentration of 1.1×10^{20} cm^{-3} and 7.3×10^{19} cm^{-3}, respectively (Figure S9). Although monolayer $GeAs_2$ exhibits higher mobility and power factor in the *a* direction, it also shows higher lattice thermal conductivity in that direction. As a result, the zT value along the *a* axis is significantly reduced. The high figure of merit for holes along the *b* axis can be attributed to the intrinsically ultralow lattice thermal conductivity of $GeAs_2$ in that direction. The undoped SnSe single crystals were reported with a room-temperature figure of merit of 0.12 along the *b* axis;[13] however, successful hole doping in single crystals of SnSe using sodium as acceptor has found a tremendous increase of zT from 0.1 to 0.7.[14] Here we demonstrate theoretically that $GeAs_2$ could be a p-type thermoelectric material as good as SnSe. GeAs has been successfully p-doped with Sn,[11] and we believe such p-doping is applicable to $GeAs_2$ as well.

With the temperature rise, the lattice thermal conductivity decreases monotonically (Figure 5a), which obeys the $1/T$ law in the regime of Umklapp phonon−phonon scatterings (see eq 8 in Methods). At 900 K the lattice thermal conductivity along the *b* axis decreases dramatically to ~0.22 W m^{-1} K^{-1}, which is

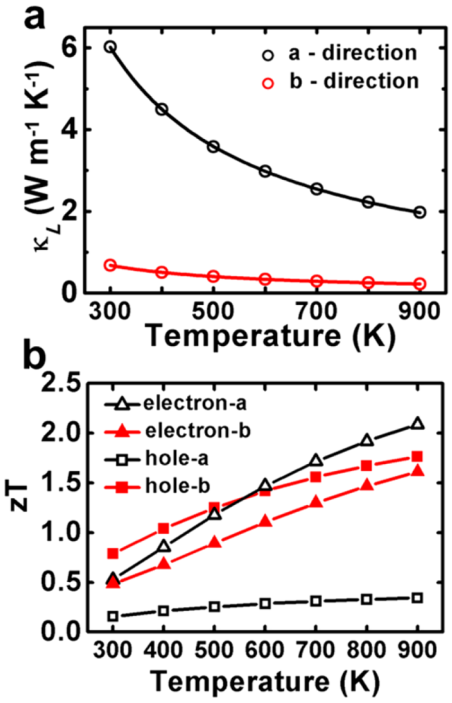

Figure 5. (a) Lattice thermal conductivity κ_L and (b) maximum thermoelectric figure of merit zT as a function of temperature for monolayer $GeAs_2$.

close to that measured for SnSe single crystals at 973 K (0.23 ± 0.03 W m^{-1} K^{-1}).[13] This is a remarkably low value considering the relatively low molecular weight of elements constituting the material. The maximum zT as a function of temperature is plotted in Figure 5b, which demonstrates a linear increase with the temperature. It should be noted that the data points in the figure are not obtained at a fixed carrier concentration; instead, they are obtained at a carrier concentration where zT maximized under every temperature, by adjusting the Fermi level in the Fermi−Dirac distribution function. The highest zT achieved at 900 K is 1.8 for p-doped monolayer $GeAs_2$ in the *b* direction and 2.1 for n-doped in the *a* direction. These values are close to those realized in unintentionally doped SnSe single crystals (p-type, 2.6 ± 0.3 at 923 K),[14] and Bi-doped SnSe single crystals (n-type, 2.2 at 773 K).[15]

CONCLUSIONS. To summarize, we theoretically demonstrate that $GeAs_2$, a IV−V group element compound with layered structure and anisotropic in-plane bonding character, possesses moderate carrier mobility, large Seebeck coefficient, and amazingly low lattice thermal conductivity in the monolayer, which make it a very promising candidate for earth-abundant thermoelectric materials. We attribute the remarkably high figure of merit of $GeAs_2$ along the *b* axis (n-type 1.6 and p-type 1.8 at 900 K) to its intrinsically ultralow lattice thermal conductivity (0.68 W m^{-1} K^{-1} at 300 K and 0.22 W m^{-1} K^{-1} at 900 K). $GeAs_2$ features soft vibrational modes and high Grüneisen parameters that reflect its anharmonic and anisotropic bonding. These unique features are responsible for the exceptionally low thermal conductivity and distinguish monolayer $GeAs_2$ from other emerging 2D materials, such as black phosphorene (110 W m^{-1} K^{-1} and 36 W m^{-1} K^{-1} in the zigzag and armchair directions at 300 K),[46] arsenene (30.4 W m^{-1} K^{-1} and 7.8 W m^{-1} K^{-1} in the zigzag and armchair directions at 300 K),[47] and monolayer MoS_2 (34.5 ± 4 W m^{-1} K^{-1} at room temperature).[48] The attributes we discovered in

DOI: 10.1021/acs.chemmater.7b01343
Chem. Mater. 2017, 29, 6261−6268

$GeAs_2$ such as layered structure, anharmonicity, and anisotropic bonding, closely resemble those of high performance thermoelectric SnSe single crystals, which puts our trust in its great potential for thermoelectric applications.

■ ASSOCIATED CONTENT

Supporting Information

The Supporting Information is available free of charge on the ACS Publications website at DOI: 10.1021/acs.chemmater.7b01343.

Additional figures and tables, computational details, and references (PDF)

■ AUTHOR INFORMATION

Corresponding Author

*(D.W.) E-mail: dong913@tsinghua.edu.cn.

ORCID

Tianqi Zhao: 0000-0002-3562-4679

Zhigang Shuai: 0000-0003-3867-2331

Author Contributions

‖(T.Z. and Y.S.) These authors contributed equally.

Author Contributions

The manuscript was written through contributions of all authors. All authors have given approval to the final version of the manuscript.

Notes

The authors declare no competing financial interest.

■ ACKNOWLEDGMENTS

This work was supported by the National Natural Science Foundation of China (Grants 21673123, 21290190, and 91333202) and the Ministry of Science and Technology of China (Grants 2013CB933503 and 2015CB655002). Computational resources were provided by the Tsinghua Supercomputing Center.

■ REFERENCES

(1) Novoselov, K. S.; Geim, A. K.; Morozov, S. V.; Jiang, D.; Zhang, Y.; Dubonos, S. V.; Grigorieva, I. V.; Firsov, A. A. Electric field effect in atomically thin carbon films. *Science* **2004**, *306*, 666−669.

(2) Li, S. L.; Tsukagoshi, K.; Orgiu, E.; Samori, P. Charge transport and mobility engineering in two-dimensional transition metal chalcogenide semiconductors. *Chem. Soc. Rev.* **2016**, *45*, 118−151.

(3) Wang, Q. H.; Kalantar-Zadeh, K.; Kis, A.; Coleman, J. N.; Strano, M. S. Electronics and optoelectronics of two-dimensional transition metal dichalcogenides. *Nat. Nanotechnol.* **2012**, *7*, 699−712.

(4) Lee, M. J.; Ahn, J. H.; Sung, J. H.; Heo, H.; Jeon, S. G.; Lee, W.; Song, J. Y.; Hong, K. H.; Choi, B.; Lee, S. H.; Jo, M. H. Thermoelectric materials by using two-dimensional materials with negative correlation between electrical and thermal conductivity. *Nat. Commun.* **2016**, *7*, 12011.

(5) Balendhran, S.; Walia, S.; Nili, H.; Sriram, S.; Bhaskaran, M. Elemental analogues of graphene: silicene, germanene, stanene, and phosphorene. *Small* **2015**, *11*, 640−652.

(6) Zhang, S.; Yan, Z.; Li, Y.; Chen, Z.; Zeng, H. Atomically thin arsenene and antimonene: semimetal-semiconductor and indirect-direct band-gap transitions. *Angew. Chem., Int. Ed.* **2015**, *54*, 3112−3115.

(7) Zeier, W. G.; Zevalkink, A.; Gibbs, Z. M.; Hautier, G.; Kanatzidis, M. G.; Snyder, G. J. Thinking like a chemist: intuition in thermoelectric materials. *Angew. Chem., Int. Ed.* **2016**, *55*, 6826−6841.

(8) Wadsten, T. The crystal structures of SiP_2, $SiAs_2$, and GeP. *Acta Chem. Scand.* **1967**, *21*, 593−594.

(9) Rau, J. W.; Kannewurf, C. R. Optical Absorption, Reflectivity, and Electrical Conductivity in GeAs and $GeAs_2$. *Phys. Rev. B: Solid State* **1971**, *3*, 2581−2587.

(10) Lee, K.; Synnestvedt, S.; Bellard, M.; Kovnir, K. GeP and $(Ge_{1-x}Sn_x)(P_{1-y}Ge_y)$ (x ≈0.12, y ≈ 0.05): Synthesis, structure, and properties of two-dimensional layered tetrel phosphides. *J. Solid State Chem.* **2015**, *224*, 62−70.

(11) Lee, K.; Kamali, S.; Ericsson, T.; Bellard, M.; Kovnir, K. GeAs: Highly Anisotropic van der Waals Thermoelectric Material. *Chem. Mater.* **2016**, *28*, 2776−2785.

(12) Barreteau, C.; Michon, B.; Besnard, C.; Giannini, E. High-pressure melt growth and transport properties of SiP, SiAs, GeP, and GeAs 2D layered semiconductors. *J. Cryst. Growth* **2016**, *443*, 75−80.

(13) Zhao, L. D.; Lo, S. H.; Zhang, Y.; Sun, H.; Tan, G.; Uher, C.; Wolverton, C.; Dravid, V. P.; Kanatzidis, M. G. Ultralow thermal conductivity and high thermoelectric figure of merit in SnSe crystals. *Nature* **2014**, *508*, 373−377.

(14) Zhao, L. D.; Tan, G.; Hao, S.; He, J.; Pei, Y.; Chi, H.; Wang, H.; Gong, S.; Xu, H.; Dravid, V. P.; Uher, C.; Snyder, G. J.; Wolverton, C.; Kanatzidis, M. G. Ultrahigh power factor and thermoelectric performance in hole-doped single-crystal SnSe. *Science* **2016**, *351*, 141−144.

(15) Duong, A. T.; Nguyen, V. Q.; Duvjir, G.; Duong, V. T.; Kwon, S.; Song, J. Y.; Lee, J. K.; Lee, J. E.; Park, S.; Min, T.; Lee, J.; Kim, J.; Cho, S. Achieving ZT = 2.2 with Bi-doped n-type SnSe single crystals. *Nat. Commun.* **2016**, *7*, 13713.

(16) Bryden, J. H. The crystal structures of the Germanium-Arsenic compounds. I. Germanium Diarsenide, $GeAs_2$. *Acta Crystallogr.* **1962**, *15*, 167−171.

(17) Kresse, G.; Furthmuller, J. Efficient iterative schemes for ab initio total-energy calculations using a plane-wave basis set. *Phys. Rev. B: Condens. Matter Mater. Phys.* **1996**, *54*, 11169−11186.

(18) Kresse, G.; Furthmuller, J. Efficiency of ab-initio total energy calculations for metals and semiconductors using a plane-wave basis set. *Comput. Mater. Sci.* **1996**, *6*, 15−50.

(19) Grimme, S.; Antony, J.; Ehrlich, S.; Krieg, H. A consistent and accurate ab initio parametrization of density functional dispersion correction (DFT-D) for the 94 elements H-Pu. *J. Chem. Phys.* **2010**, *132*, 154104.

(20) Heyd, J.; Scuseria, G. E.; Ernzerhof, M. Hybrid functionals based on a screened Coulomb potential. *J. Chem. Phys.* **2003**, *118*, 8207.

(21) Giannozzi, P.; Baroni, S.; Bonini, N.; Calandra, M.; Car, R.; Cavazzoni, C.; Ceresoli, D.; Chiarotti, G. L.; Cococcioni, M.; Dabo, I.; Dal Corso, A.; de Gironcoli, S.; Fabris, S.; Fratesi, G.; Gebauer, R.; Gerstmann, U.; Gougoussis, C.; Kokalj, A.; Lazzeri, M.; Martin-Samos, L.; Marzari, N.; Mauri, F.; Mazzarello, R.; Paolini, S.; Pasquarello, A.; Paulatto, L.; Sbraccia, C.; Scandolo, S.; Sclauzero, G.; Seitsonen, A. P.; Smogunov, A.; Umari, P.; Wentzcovitch, R. M. QUANTUM ESPRESSO: a modular and open-source software project for quantum simulations of materials. *J. Phys.: Condens. Matter* **2009**, *21*, 395502.

(22) Poncé, S.; Margine, E. R.; Verdi, C.; Giustino, F. EPW: Electron−phonon coupling, transport and superconducting properties using maximally localized Wannier functions. *Comput. Phys. Commun.* **2016**, *209*, 116−133.

(23) Marzari, N.; Mostofi, A. A.; Yates, J. R.; Souza, I.; Vanderbilt, D. Maximally localized Wannier functions: Theory and applications. *Rev. Mod. Phys.* **2012**, *84*, 1419−1475.

(24) de Koker, N. Thermal conductivity of MgO periclase from equilibrium first principles molecular dynamics. *Phys. Rev. Lett.* **2009**, *103*, 125902.

(25) Morelli, D. T.; Heremans, J. P.; Slack, G. A. Estimation of the isotope effect on the lattice thermal conductivity of group IV and group III-V semiconductors. *Phys. Rev. B: Condens. Matter Mater. Phys.* **2002**, *66*, 195304.

(26) Mounet, N.; Marzari, N. First-principles determination of the structural, vibrational and thermodynamic properties of diamond, graphite, and derivatives. *Phys. Rev. B: Condens. Matter Mater. Phys.* **2005**, *71*, 205214.

DOI: 10.1021/acs.chemmater.7b01343
Chem. Mater. 2017, 29, 6261−6268

(27) Togo, A.; Tanaka, I. First principles phonon calculations in materials science. *Scr. Mater.* **2015**, *108*, 1−5.
(28) Janesko, B. G.; Henderson, T. M.; Scuseria, G. E. Screened hybrid density functionals for solid-state chemistry and physics. *Phys. Chem. Chem. Phys.* **2009**, *11*, 443−454.
(29) Novoselov, K. S.; Jiang, D.; Schedin, F.; Booth, T. J.; Khotkevich, V. V.; Morozov, S. V.; Geim, A. K. Two-dimensional atomic crystals. *Proc. Natl. Acad. Sci. U. S. A.* **2005**, *102*, 10451−10453.
(30) Coleman, J. N.; Lotya, M.; O'Neill, A.; Bergin, S. D.; King, P. J.; Khan, U.; Young, K.; Gaucher, A.; De, S.; Smith, R. J.; Shvets, I. V.; Arora, S. K.; Stanton, G.; Kim, H. Y.; Lee, K.; Kim, G. T.; Duesberg, G. S.; Hallam, T.; Boland, J. J.; Wang, J. J.; Donegan, J. F.; Grunlan, J. C.; Moriarty, G.; Shmeliov, A.; Nicholls, R. J.; Perkins, J. M.; Grieveson, E. M.; Theuwissen, K.; McComb, D. W.; Nellist, P. D.; Nicolosi, V. Two-dimensional nanosheets produced by liquid exfoliation of layered materials. *Science* **2011**, *331*, 568−571.
(31) Sachs, B.; Wehling, T. O.; Novoselov, K. S.; Lichtenstein, A. I.; Katsnelson, M. I. Ferromagnetic two-dimensional crystals: Single layers of K_2CuF_4. *Phys. Rev. B: Condens. Matter Mater. Phys.* **2013**, *88*, 201402.
(32) Shulenburger, L.; Baczewski, A. D.; Zhu, Z.; Guan, J.; Tomanek, D. The Nature of the Interlayer Interaction in Bulk and Few-Layer Phosphorus. *Nano Lett.* **2015**, *15*, 8170−8175.
(33) Desai, S. B.; Madhvapathy, S. R.; Sachid, A.; Llinas, J. P.; Wang, Q.; Ahn, G. H.; Pitner, G.; Kim, M. J.; Bokor, J.; Hu, C.; Wong, H.-S. P.; Javey, A. MoS_2 transistors with 1-nanometer gate lenghts. *Science* **2016**, *354*, 99−102.
(34) Kanazawa, T.; Amemiya, T.; Ishikawa, A.; Upadhyaya, V.; Tsuruta, K.; Tanaka, T.; Miyamoto, Y. Few-layer HfS_2 transistors. *Sci. Rep.* **2016**, *6*, 22277.
(35) Das, S.; Chen, H. Y.; Penumatcha, A. V.; Appenzeller, J. High performance multilayer MoS_2 transistors with scandium contacts. *Nano Lett.* **2013**, *13*, 100−105.
(36) Roldan, R.; Castellanos-Gomez, A.; Cappelluti, E.; Guinea, F. Strain engineering in semiconducting two-dimensional crystals. *J. Phys.: Condens. Matter* **2015**, *27*, 313201.
(37) Zhu, C. R.; Wang, G.; Liu, B. L.; Marie, X.; Qiao, X. F.; Zhang, X.; Wu, X. X.; Fan, H.; Tan, P. H.; Amand, T.; Urbaszek, B. Strain tuning of optical emission energy and polarization in monolayer and bilayer MoS_2. *Phys. Rev. B: Condens. Matter Mater. Phys.* **2013**, *88*, 121301.
(38) Conley, H. J.; Wang, B.; Ziegler, J. I.; Haglund, R. F., Jr.; Pantelides, S. T.; Bolotin, K. I. Bandgap engineering of strained monolayer and bilayer MoS_2. *Nano Lett.* **2013**, *13*, 3626−3630.
(39) Mak, K. F.; Lee, C.; Hone, J.; Shan, J.; Heinz, T. F. Atomically thin MoS_2: a new direct-gap semiconductor. *Phys. Rev. Lett.* **2010**, *105*, 136805.
(40) Bardeen, J.; Shockley, W. Deformation Potentials and Mobilities in Non-Polar Crystals. *Phys. Rev.* **1950**, *80*, 72−80.
(41) Long, M.-Q.; Tang, L.; Wang, D.; Shuai, Z. Theoretical predictions of size-dependent carrier mobility and polarity in graphene. *J. Am. Chem. Soc.* **2009**, *131*, 17728−17729.
(42) Long, M.-Q.; Tang, L.; Wang, D.; Li, Y.; Shuai, Z. Electronic structure and carrier mobiity in graphdiyne sheet and nanoribbons: theoretical predictions. *ACS Nano* **2011**, *5*, 2593−2600.
(43) Cai, Y.; Zhang, G.; Zhang, Y. W. Polarity-reversed robust carrier mobility in monolayer MoS_2 nanoribbons. *J. Am. Chem. Soc.* **2014**, *136*, 6269−6275.
(44) Qiao, J.; Kong, X.; Hu, Z. X.; Yang, F.; Ji, W. High-mobility transport anisotropy and linear dichroism in few-layer black phosphorus. *Nat. Commun.* **2014**, *5*, 4475.
(45) Dai, J.; Zeng, X. C. Titanium trisulfide monolayer: theoretical prediction of a new direct-gap semiconductor with high and anisotropic carrier mobility. *Angew. Chem., Int. Ed.* **2015**, *54*, 7572−7576.
(46) Jain, A.; McGaughey, A. J. H. Strongly anisotropic in-plane thermal transport in single-layer black phosphorene. *Sci. Rep.* **2015**, *5*, 8501.
(47) Zeraati, M.; Vaez Allaei, S. M.; Abdolhosseini Sarsari, I.; Pourfath, M.; Donadio, D. Highly anisotropic thermal conductivity of arsenene: An ab initio study. *Phys. Rev. B: Condens. Matter Mater. Phys.* **2016**, *93*, 085424.
(48) Yan, R.; Simpson, J. R.; Bertolazzi, S.; Brivio, J.; Watson, M.; Wu, X.; Kis, A.; Luo, T.; Hight Walker, A. R. H.; Xing, H. G. Thermal conductivity of monolayer molybdenum disulfide obtained from temperature-dependent Raman spectroscopy. *ACS Nano* **2014**, *8*, 986−993.

DOI: 10.1021/acs.chemmater.7b01343
Chem. Mater. 2017, 29, 6261−6268